



Numerical simulation on the dynamic mechanical response and fracture mechanism of rocks containing a single hole

Zhenyu Han^{1,3} · Kai Liu² · Jinyin Ma³ · Diyuan Li³

Received: 24 August 2023 / Revised: 10 November 2023 / Accepted: 24 June 2024
© The Author(s) 2024

Abstract

Caverns and tunnels are constantly exposed to dynamic loads, posing a potentially significant threat to the safety of rock structures. To facilitate the understanding of dynamic fracture around openings, a series of discrete element models were established to numerically examine the effect of hole shape on dynamic mechanical properties and crack evolution. The results indicate that the existence of a hole greatly reduces dynamic strength, and the reduction is closely related to hole shape. The strain variation of pre-holed specimens is more complicated and even larger than the value of intact specimens. Although crack initiation differs for varying hole shapes, the entire structural collapse of specimens is controlled by macro shear cracks along the diagonal direction of the specimen, which are effectively identified by velocity trend arrows and contact force distribution. Finally, comparative analysis between failure pattern of pre-holed specimens under static and dynamic loads were conducted.

Keywords Hole · Rock dynamics · PFC · Crack propagation · Mechanical response

1 Introduction

With the population explosion, urban land scarcity and mineral resource shortage are becoming increasingly severe, which imminently requires developing more underground space to accommodate huge human beings and exploiting deep resources to maintain the normal operation of society (Xie et al. 2021). On one hand, an enormous number of underground caverns and tunnels are expected to be excavated in the near future (Fig. 1a), and their stability and safety during construction and operation are of essential importance to economic benefits and staff's lives. On the other hand, a mass of open goafs are left for some rock projects (Fig. 1b), like mining, bringing many geohazards, such as

spalling, rockburst and ground subsidence. Hence, it is crucially significant to deeply and comprehensively understand the underlying fracture mechanism of surrounding rocks of cavities, which can provide scientific guidance for design, construction, evaluation and maintenance of subsurface structures.

The studies on mechanical response of rocks containing a hole start from theoretical derivation. As long ago as 1913, analytical solutions of stress concentration factor along a circular or elliptical hole were obtained by Inglis (1913) using elasticity theory. For a plate containing a circular hole under remote biaxial compression, Sammis and Ashby (1986) calculated the local stress field and further predicted the crack growth paths from the hole. Zhao et al. (2011) modified the Sammis–Ashby model and found the relationship between uniaxial compressive strength (UCS) and the pre-hole radius. Considering the effect of a variety of hole shapes, the stress distributions around a pre-hole were derived (Sharma 2012; Tan et al. 2021b; Wu et al. 2020; Zhao and Yang 2015) using complex variable theory, and they also found that arched edges can bear large external loads owing to a small stress concentration. The solution of Carter et al. (1992) also incorporated the effect of confining pressure. As the material is anisotropic, a unified semi-analytical solution was put forward by Setiawan and Zimmerman (2020)

✉ Zhenyu Han
zhenyu_han@seu.edu.cn

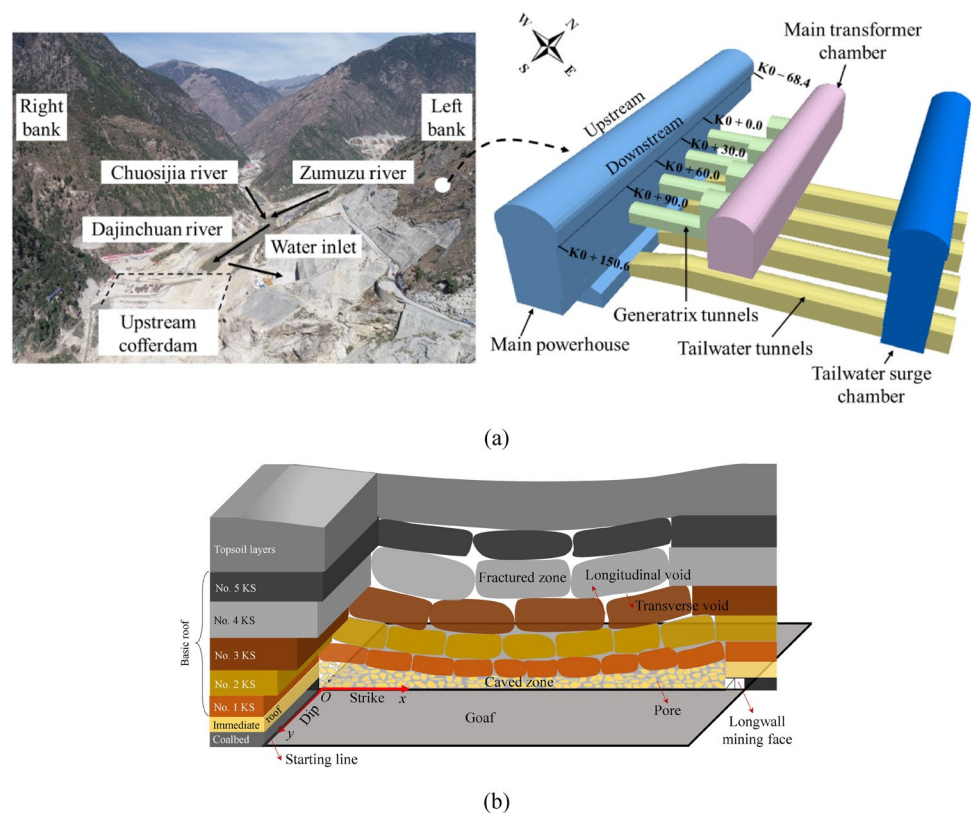
✉ Kai Liu
kai.liu@eng.ox.ac.uk

¹ Department of Civil Engineering, Monash University, Melbourne, VIC 3800, Australia

² Department of Engineering Science, University of Oxford, Parks Road, Oxford OX1 3PJ, UK

³ School of Resources and Safety Engineering, Central South University, Changsha 410083, Hunan, China

Fig. 1 **a** Underground caverns of the Shuangjiangkou Hydropower Station (Xia et al. 2023) and **b** Schematic of underground goaf (Wang and Li 2017)



to determine the magnitude and direction of stress field. Furthermore, an improved Schwarz alternating method was proposed to obtain the stress solution near the double pre-holes with a U-shape (Tan et al. 2021a). In addition, the interaction mechanism between holes in circular (Kooi and Verrijt 2001; Ukadgaonker 1980) and elliptical shapes (Zhang et al. 2003) were analytically explored as well. These findings have laid a solid foundation for revealing the fracture mechanism around the holes, however, which also requires laboratory tests to validate analytical solutions. In addition, according to the principle of similarity, the underground caverns and tunnels are usually simplified as prefabricated holes embedded in brittle rock and rock-like materials (Jongpradist et al. 2015), and new experimental phenomena can also provide new insights into theoretical analysis in turn. In the past century, a large number of experiments were carried out to examine the mechanical response and fracture behavior of pre-holed brittle materials. Under compression, the ultimate failure mode around a circular hole exhibited slabbing fractures approximately along the direction of the maximum compressive stress, which were caused by the combination of primary and remote cracks (Carter et al. 1991, 1992). With the aid of digital image correlation (DIC) technique, Li et al. (2017) experimentally examined the fracture process of Carrara marble containing a circular or elliptical hole. Their findings revealed that the primary cracks causing the final failure were highly sensitive to the development

of strain localized bands. Zeng et al. (2018) compared the strength and deformation characteristics of sandstone with a various-shaped hole, and they pointed the shape effect on the UCS was considerable but on the Young's modulus was insignificant. Under biaxial compression, it was found that tensile cracks played a key role in the structural collapse at low confining pressure, but the compressive concentrations became the dominant factor for failure at a high confining pressure (Fakhimi et al. 2002; Lajtai and Lajtai 1975). Tan et al. (2022) studied the effect of multiple holes on the mechanical response and crack evolution of marble. Their results indicated that high compressive stress around one hole was more likely to restrict the tensile crack growth from other two holes. Yang et al. (2019), Mahmoodzadeh et al. (2022), Zhang et al. (2022a), and Ai and Gao (2023) investigated the interaction mechanism between joints and the hole through experimental and numerical approaches.

Laboratory test is an effective method to study the crack evolution in brittle materials, but it is usually highly expensive and time-consuming. Plus, the implementation of experimental investigations from a mesoscopic perspective requires advanced precision instruments, such as the synchrotron CT imaging apparatus and scanning electron microscope (SEM). The advancement of numerical simulation in recent decades has made it a powerful tool to mimic the fracture process of brittle materials, which has been successfully applied and attracted extensive attention in rock mechanics

and fracture mechanics. Through a finite element package in ANSYS, the principal stress distribution were calculated to shed light on the stress concentration point under uniaxial and biaxial compression (Carter et al. 1991). Zhao et al. (2023) adopted PFC^{2D} to reproduce the spalling behavior in the rectangular cavity, and the size effect of cavity was also examined. Zhang et al. (2022b) extracted the strain values of several feature points near a singular square opening by RFPA^{2D}, which showed that tensile cracks tended to emanate at the upper and lower edges of the opening. The crack propagation paths were also successfully conducted for a pre-hole with other cross-section shapes embedded in brittle specimens, such as elliptical and diamond (Zeng et al. 2018). Since the joints in rock masses cannot be neglected, PFC^{2D} simulation results indicated that the failure process around a circular hole is progressive at a low joint angle but a sudden rupture at a high joint angle, and the increasing angle led to the contraction of damage area around the hole (Sagong et al. 2011). Using PFC^{2D}, the effects of the stress state and the inclination angle of an elliptical pre-hole were also numerically studied (Zhang et al. 2023). In addition, anisotropy was also added to a distinct element model using discrete fracture network (DFN) in UDEC^{2D}, whose prominent effect on the induced stress near the hole was verified by Karimi-Khajelangi and Noorian-Bidgoli (2022). Through FLAC^{2D} and PLAXI^{2D}, Kooi and Verruijt (2001) found that the displacement of the interaction area between double circular holes were significantly enhanced. Thereafter, stress and displacement vector fields were further numerically obtained to clarify the coalescence mechanism among multi cavities (Abharian et al. 2022; Huang et al. 2017; Li et al. 2021; Liu et al. 2020; Tan et al. 2021a, 2022; Zhao et al. 2021).

Most of the current research were concentrated on the mechanical behavior under quasi-static loads. Nonetheless, rock engineering is always practically subjected to dynamic loads in the excavation process, such as blasting, machine vibration and seismic activities (Han et al. 2022, 2023; Li et al. 2022, 2023a). On account of this, after numerous investigations, it has been widely accepted that dynamic mechanical properties are remarkably enhanced owing to the increasing strain rate (Mahanta et al. 2017; Ramesh et al. 2015). With regard to fracture dynamics, researchers and scholars paid more attention to the cracking extension from “crack-like” flaws (Han et al. 2022b; Li et al. 2019; Yan et al. 2021; Zou et al. 2021). It is found that the existence of pre-flaws reduced the dynamic strength, and the reduction was dependent on the flaw configuration, confining pressure, water content, etc. (Zhou et al. 2021). Shear cracks were observed to be initiate firstly, and tensile cracks were suppressed owing to the strain rate localization (Zou et al. 2021). Some efforts were also made to explore the cracking behavior around circular and elliptical holes (Han et al.

2022a; Li et al. 2023b; Tao et al. 2020, 2022; Weng et al. 2017), and their results confirmed the significant influence of hole inclination.

Previous achievements have greatly facilitated the research progress on the damage mechanism of flawed rock and rock-like specimens. However, there are a variety of shapes for the cross-section of tunnels and chambers apart from round shapes, whose dynamic response is still unclear. Hence, this study is attempted to systemically examine the effect of hole shape on the dynamic mechanical properties, cracking process and failure mechanism using a discrete element method (DEM).

2 Numerical model

2.1 Brief description of PFC

The discrete element method (DEM), possessing a unique advantage in simulating brittle crack propagation, has been widely recognized and applied in the field of rock fracture mechanics (Abharian et al. 2022; Khazaei et al. 2015; Poulsen et al. 2018; Zhang et al. 2020). At present this method has become a mainstream approach for reproducing the crack initiation, growth, coalescence and final failure. In this study, a popular DEM code, two-dimensional particle flow code (PFC^{2D}) is adopted to conduct the numerical simulation, in which the model consists of a gathering of rigid particles at various sizes, and the interaction among particles is conveyed through contacts. The iterative calculations adhere to Newton's second law for particles and a force–displacement law for in-built contacts.

2.2 Model setup

2.2.1 SHPB apparatus

The numerical model of SHPB apparatus is established according to Han et al. (2022b), where the length of incident bar, transmitted bar and striker is 2000 mm, 1500 mm and 200 mm, respectively, with a fixed diameter of 50 mm, as illustrated in Fig. 2, and their particles are selected to be a diameter of 1.25 mm with the contact bond model (CBM) applied. To achieve the dynamic stress balance and a constant strain rate, a pulse shaper with the diameter × thickness of 25 mm × 3 mm is attached on the incident bar to reduce wave oscillation. To ensure the high stiffness and elasticity of the steel bars in the entire loading process, the contact bond strength is set at an extremely large value. Two measurement circles are set in the bar centers to monitor and record the stress and strain waveforms. The minimum radius of specimen particles is set the same as that of the particles on the bar-specimen ends to ensure a satisfactory contact

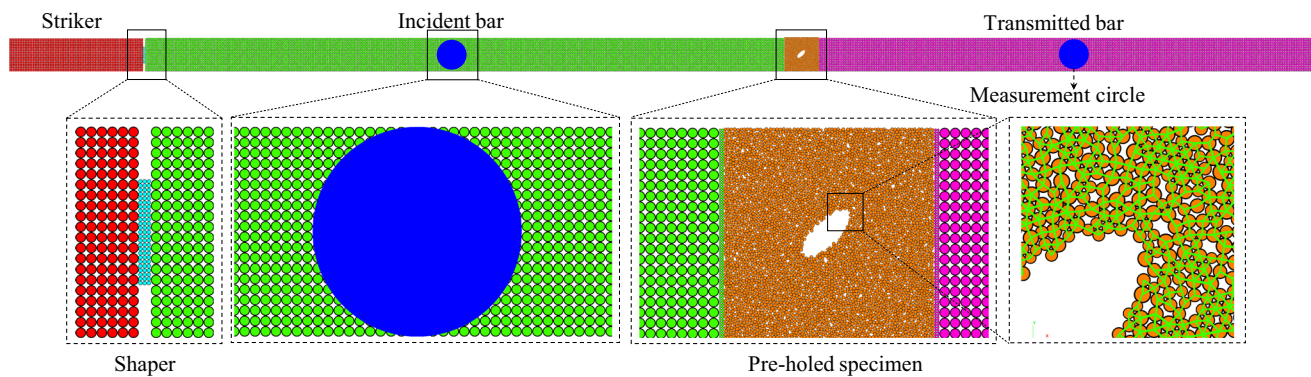


Fig. 2 Numerical model of SHPB apparatus with a pre-holed specimen sandwiched

Table 1 Micro parameters of the SHPB apparatus in the PFC model (Yuan et al. 2020)

Micro parameters	Values
Particle radius (mm)	1.25
Density (kg/m^3)	7894.7
Contact modulus of the particle (GPa)	200
Contact bond gap (mm)	0.001
Normal contact stiffness (N/m)	6.86×10^{11}
Shear contact stiffness (N/m)	2.45×10^{11}
Normal strength (Pa)	1.0×10^{100}
Shear strength (Pa)	1.0×10^{100}

condition. After a trial-and-error process, the detailed micro parameters of the SHPB apparatus are listed in Table 1. During the tests, the high-strength striker is launched to impact the incident bar at a high velocity. A half-sine stress wave is thus generated and propagate along the loading direction. When the stress wave arrives at the incident bar end, a portion is employed to destroy the sandwiched specimen, and the other portion is reflected back to the incident bar and transmitted into the transmitted bar, acting as the useless energy finally.

2.2.2 Specimen configurations

The specimen size in this simulation study was $50 \text{ mm} \times 50 \text{ mm}$, and a single hole with various geometric shapes was created in the specimen center by deleting the particles in the hole area, as illustrated in Fig. 3a, where the side length of the square, the diameter of the circle, the median of the trapezoid, the long axis of the ellipse, and the base line and the height of the arch was 15 mm, and the height of the trapezoid and the short axis of the ellipse were 10 mm and 6 mm, respectively. The

inclination angle between the long axis of the ellipse and the loading direction was denoted as α , from 0° to 90° at an interval of 15° . Since the parallel bond model (PBM) is able to transfer force and moment, it is more suitable to simulate rock materials, which was employed in this study. As shown in Fig. 2, the top and bottom edges of the specimen model are in a free-boundary condition. Parameter calibration is normally the precondition for the reliability of numerical results. Herein, the micro parameters of sandstone specimens in were employed, as listed in Table 2, where the numerical and experimental results of a specimen under uniaxial static compression agreed well, as shown in Fig. 4.

3 Validity of the numerical model

3.1 Stress wave propagation

Figure 5 illustrates the stress wave propagation within the specimen and steel bars under a impact velocity of 10 m/s. As the striker impacted the incident bar through the pulse shaper, a compressive stress wave is generated and then propagated along the impact direction. Upon reaching the sandwiched specimen, a portion of the stress wave is reflected back to the incident bar in a form of tensile stress wave, while the remainder continues to propagate into the transmitted bar via the specimen. During this process, the stress wave propagation adheres to the principles of one-dimensional stress wave theory.

3.2 Dynamic stress balance

A pulse shaper was adopted in the simulation to help generate a ramp incident stress wave lasting approximately $250 \mu\text{s}$. This duration allows for sufficient time for the wave to reverberate within the specimen and attain a state of dynamic stress

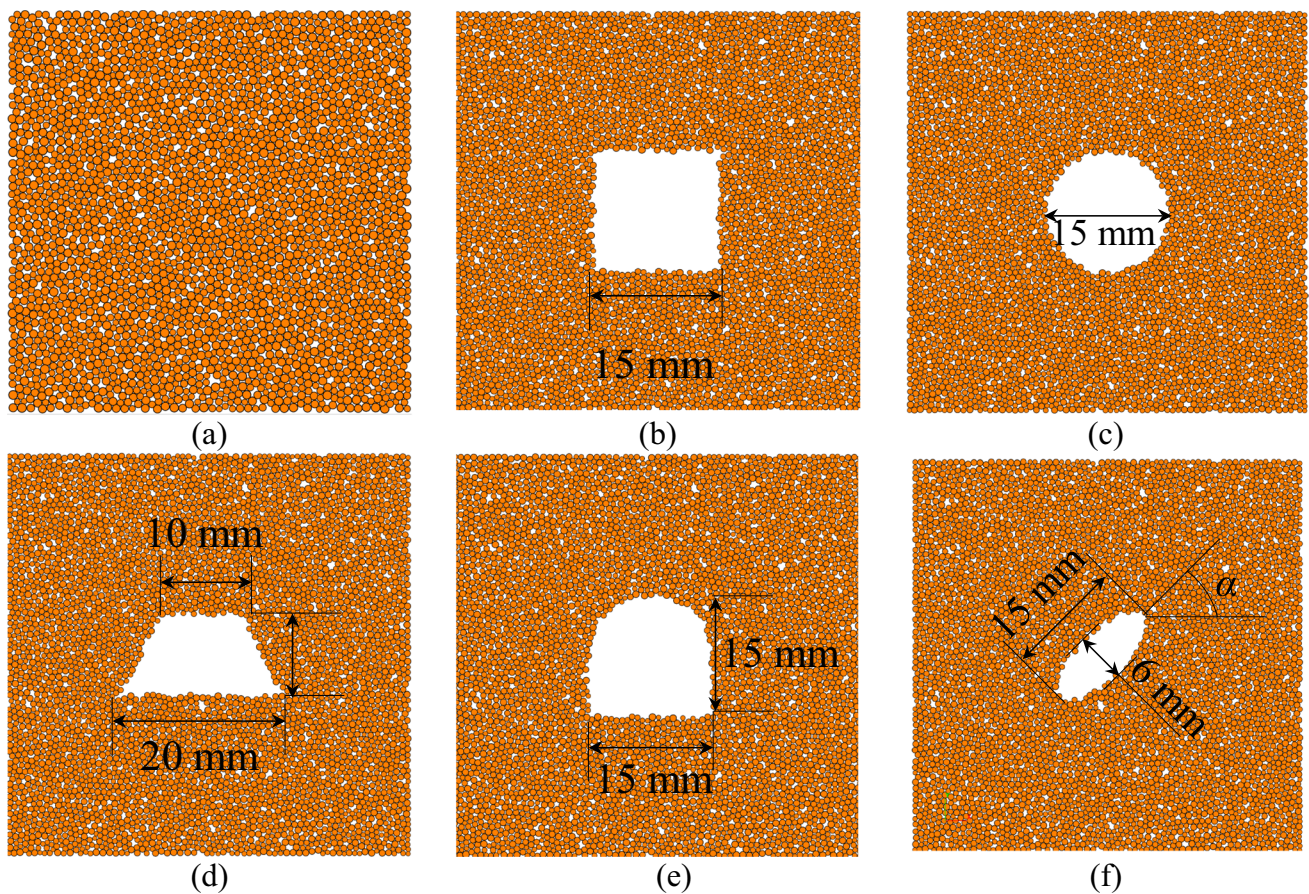


Fig. 3 a Intact specimen and b–f Specimens containing a square, circular, trapezoidal, arched and elliptical ($\alpha=45^\circ$) hole, respectively

Table 2 Micro parameters of sandstone specimens (Zhang and Wang 2018)

Micro parameter	Value
Particle radius (mm)	1.25
Density (kg/m^3)	7894.7
Contact modulus of the particle (GPa)	200
Contact bond gap (mm)	0.001
Normal contact stiffness (N/m)	6.86×10^{11}
Shear contact stiffness (N/m)	2.45×10^{11}
Normal strength (Pa)	1.0×10^{100}
Shear strength (Pa)	1.0×10^{100}

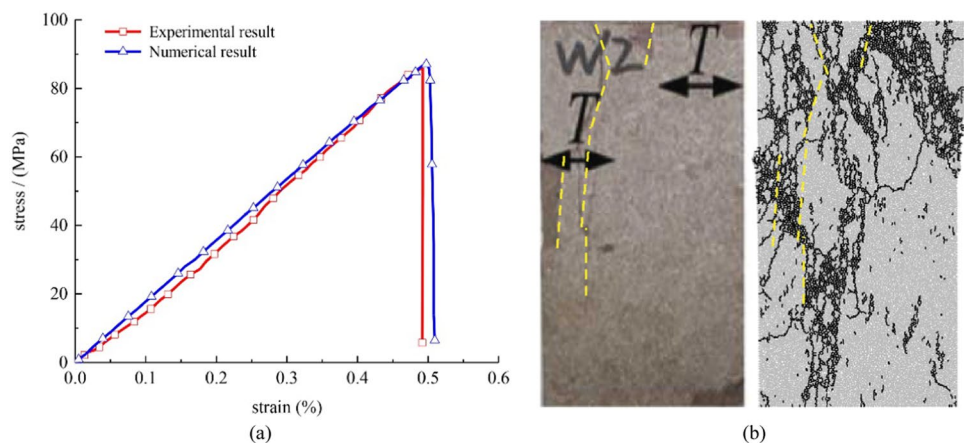
equilibrium, which is the precondition for obtaining precise and dependable numerical outcomes. After reflection and transmission, original waveforms were recorded by measurement circles and depicted in Figs. 6a and b, where all three waves exhibit a gradual rise in amplitude with minimal oscillation. The stresses at both the incident and transmitted ends of the specimen were also monitored, and their relationships

with time for an intact specimen and a representative pre-holed specimen are shown in Figs. 6c and d. At the loading onset, the stress (Inc. stress) at the incident end was obvious larger than the counterpart (Tra. stress) at the transmitted end. Following multiple wave reverberations, the dynamic stresses at both ends were roughly equivalent to each other, particularly prior to reaching peak values. This signifies that dynamic stress equilibrium was successfully accomplished in our numerical study. Moreover, a stress equilibrium factor η was defined to evaluate the quality of stress equilibrium, expressed as follows (Li et al. 2014):

$$\eta = 2 \frac{\sigma_{\text{Inc.}} + \sigma_{\text{Re.}} - \sigma_{\text{Tra.}}}{\sigma_{\text{Inc.}} + \sigma_{\text{Re.}} - \sigma_{\text{Tra.}}} \quad (1)$$

The closer this factor is to zero, the better the stress balance is. As can be seen in Fig. 6c and d, the stress equilibrium factor exhibits a plateau that approaches zero, indicating that dynamic stress equilibrium factor was well-achieved to ensure the reliability of numerical results. Then the time-varying dynamic uniaxial strength $\sigma(t)$, axial strain rate $\dot{\epsilon}(t)$ and axial

Fig. 4 Numerical and experimental **a** Stress–strain curves and **b** Failure modes of sandstone under static uniaxial compression (Zhang and Wang 2018)



strain $\varepsilon(t)$ can be calculated as presented below (Han et al. 2020):

$$\sigma(t) = \frac{A_e E_e}{2A_s} [\varepsilon_I(t) + \varepsilon_R(t) + \varepsilon_T(t)] \quad (2)$$

$$\dot{\varepsilon}(t) = \frac{C_e}{L_s} [\dot{\varepsilon}_I(t) - \dot{\varepsilon}_R(t) - \dot{\varepsilon}_T(t)] \quad (3)$$

$$\varepsilon(t) = \frac{C_e}{L_s} \int_0^t [\varepsilon_I(t) - \varepsilon_R(t) - \varepsilon_T(t)] dt \quad (4)$$

where A_e , E_e and C_e are the cross-sectional area, P-wave velocity and Young's modulus of elastic steel bars, respectively. A_s and L_s are the cross-sectional area and height of

the specimen, respectively. $\varepsilon_I(t)$, $\varepsilon_R(t)$ and $\varepsilon_T(t)$ are incident, reflected and transmitted strain pulses, respectively.

4 Numerical results

4.1 Dynamic mechanical properties

Figure 7a depicts the dynamic stress histories of both intact and pre-holed specimens. Notably, it is apparent that the curve morphology remains consistent across all hole shapes, albeit with different degrees of strength reduction. Owing to the brief duration of dynamic loading, microcracks are unable to undergo sufficient closure, thereby resulting in the dynamic stress–strain curve directly entering the linear elastic phase. Thereafter, original cracks start to expand and

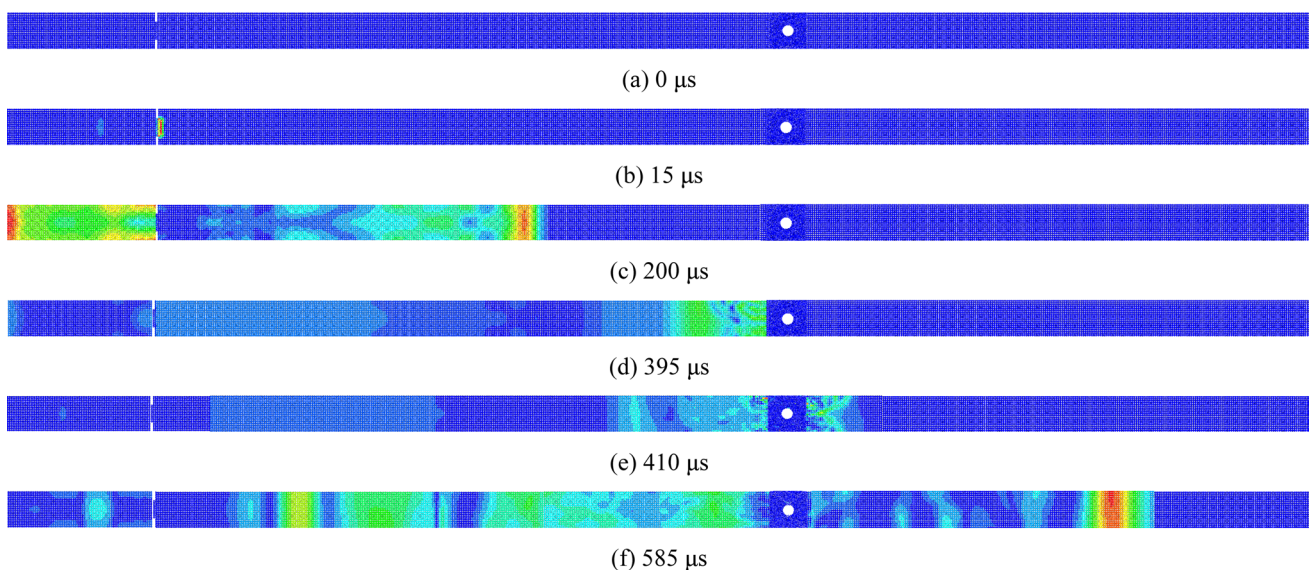


Fig. 5 Stress wave propagation in the specimen and steel bars

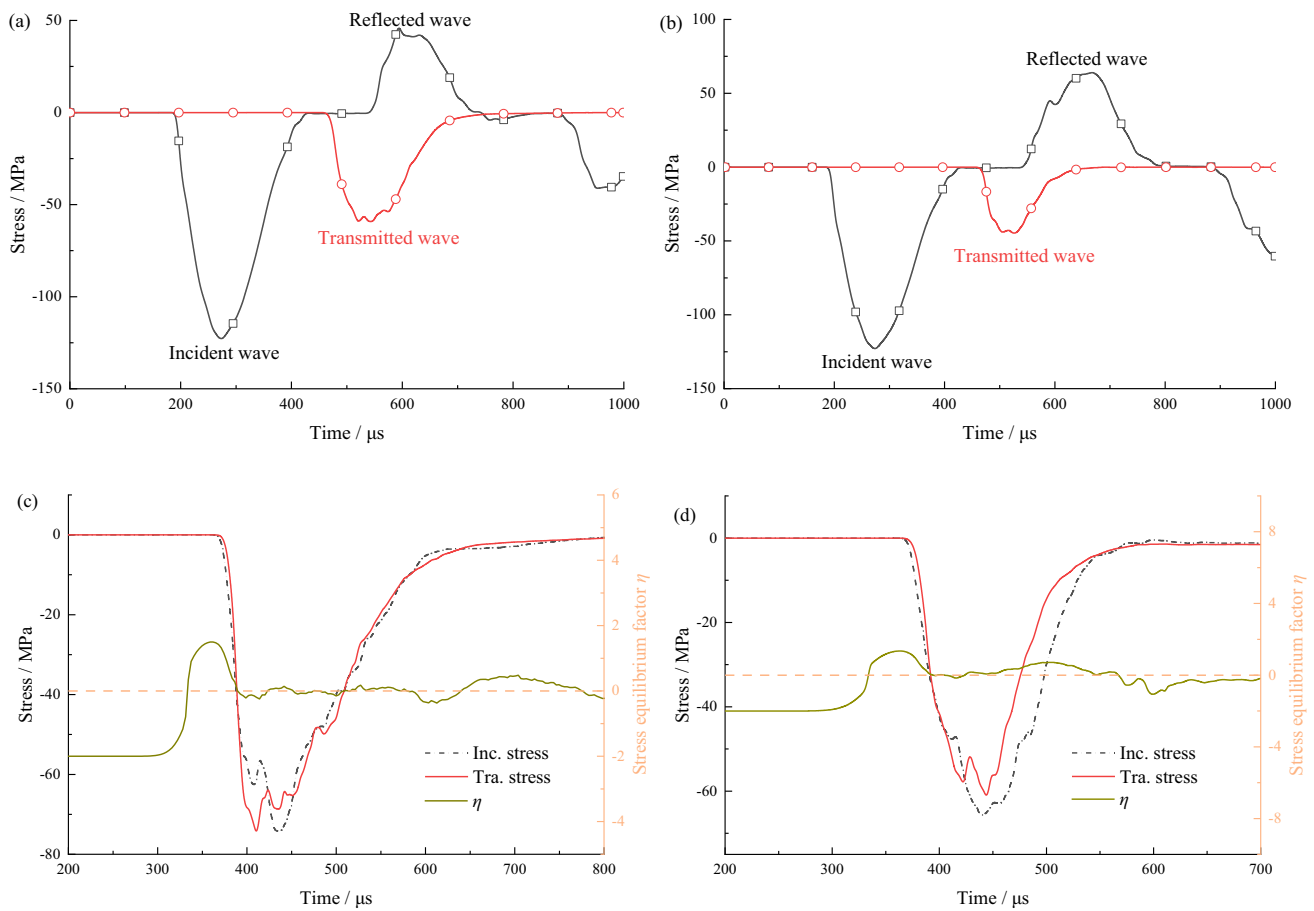


Fig. 6 **a** and **b** Typical waveforms and **c** and **d** Dynamic stress equilibrium of an intact specimen a specimen containing a 45° elliptical hole, respectively. (Inc. stress and Tra. stress denote the dynamic stress at the incident and transmitted ends, respectively.)

new cracks also emanate and develop. After exceeding its maximum threshold, the dynamic stress triggers a decline in the curve, ultimately leading to irreversible damage of the specimen.

To further examine the dynamic mechanical properties, Figs. 7b–d illustrate the dynamic uniaxial compressive strength and peak strain as a function of the hole shape of tested specimens. As shown in Fig. 7b and c, the dynamic strength of an intact specimen is 59.96 MPa, and the existence of a hole lead to a remarkable reduction. The specimen containing a 15° elliptical hole possesses the largest peak strength of 46.19 MPa, whereas the specimen with a square hole has the smallest strength at 31.37 MPa. Although the side length of the square hole is equal to the diameter of the circular hole, due to a smaller stress concentration at smooth edges, the dynamic strength of the former is smaller than that of the latter. The strength of specimens containing an arched hole is comparable to that of specimens containing a square hole. Apart from elliptical-holed specimens, those with a trapezoidal hole

exhibit the highest dynamic strength due to its small area. The relationship between dynamic strength and hole area is presented in Fig. 7c, which shows that there is a linear decreasing trend in dynamic strength with increasing hole area. For specimens containing an elliptical hole, as the inclination angle becomes larger, the dynamic strength first increases and then decreases, reaching the maximum value at 15°.

The effect of hole shape on the peak strain at the peak stress is depicted in Fig. 7d. It is evident that the peak strain of the intact specimen is 0.0682%. Upon embedding a circular hole, the peak strain increases to 0.0780%, followed by the values of 0.0591% and 0.0583% for trapezoidal and square holed specimens, respectively. Notably, specimens containing an arched hole exhibit a minimum peak strain value of 0.0180%, which is significantly lower than that of other specimens, accounting for only 26.39% of that of an intact specimen. This is the reason why this shape is widely employed in tunnels and roadways. For specimens containing an elliptical hole, the peak strain displays a reversed

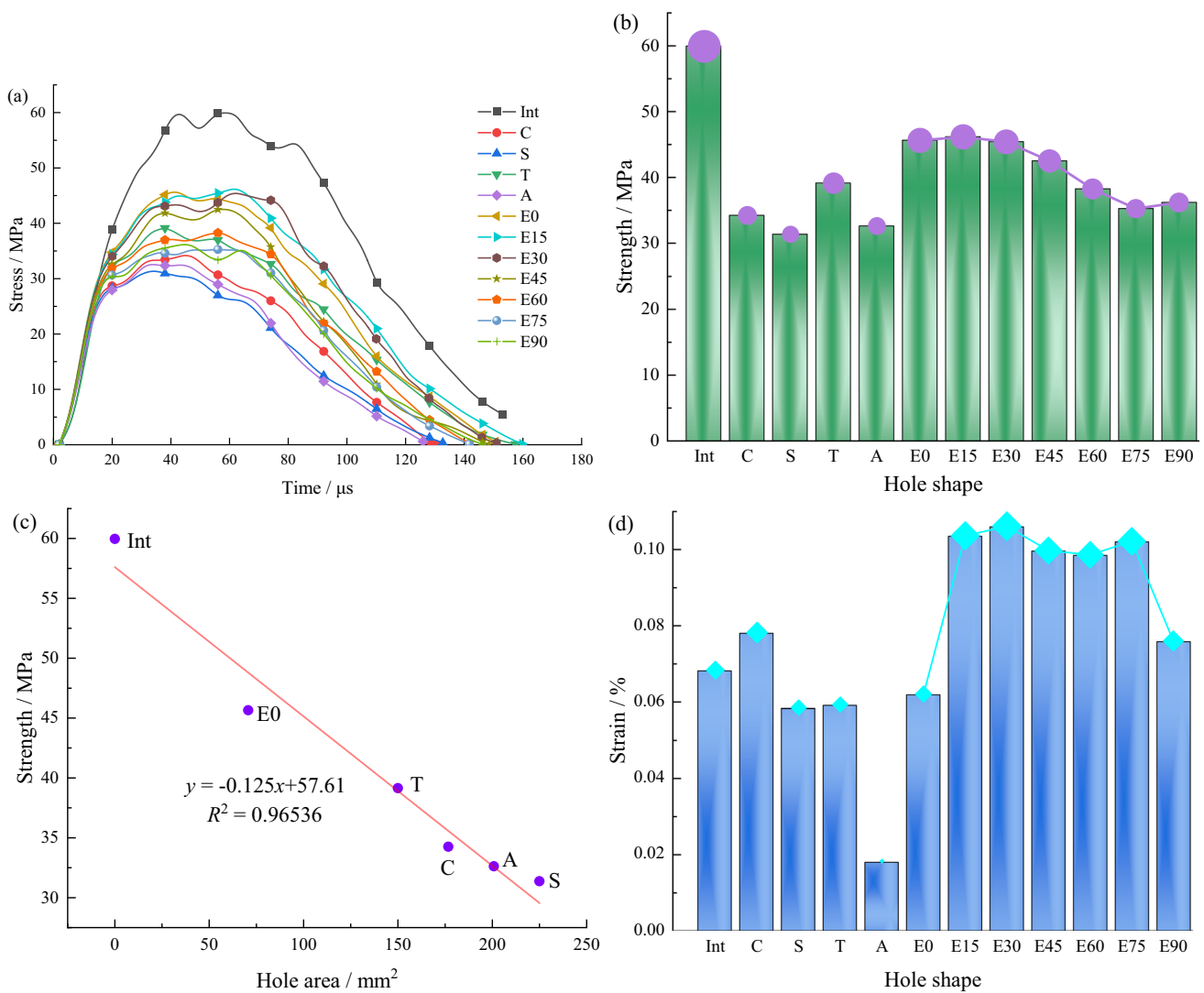


Fig. 7 **a** Dynamic stress histories, **b** and **c** Dynamic uniaxial compressive strength, and **d** Peak strain of intact and pre-holed specimens (Int, C, S, T, A and E45 are abbreviations of Intact, Circle, Square, Trapezoidal, Arched, and 45°-elliptical hole, respectively)

U-shaped variation trend with respect to inclination angle. For inclination angles between 15° and 75°, peak strain remains at a similar level that exceeds the failure strain of an intact specimen. When the long axis of the elliptical hole is parallel and perpendicular to the impact loading direction ($\alpha=0^\circ$ and 90°), peak strain is significantly reduced compared to specimens containing an inclined elliptical hole, and possesses a similar value to those squared- and trapezoidal- holed specimens.

4.2 Dynamic fracture process and AE reaction

Figure 8a illustrates the dynamic stress evolution and corresponding acoustic emission (AE) characteristics of specimens containing a circle, square, trapezoidal and arched

hole, respectively, where $F(\tau_i)$ represents the mean frequency of AE event generation within a sequence of N consecutive events, which can be obtained by Eq. (5):

$$F(\tau_i) = \frac{N}{t_{N+i-1} - t_{i-1}} \quad (5)$$

where t_i is the specific moment when the AE event occurs. The resultant displacement contours at five featured stresses (①–⑤) are plotted in Fig. 8b. Figure 8a reveals that only a few AE events are generated in the initial loading stage, as the specimen undergoes elastic deformation at this stage. Point ② further demonstrates that larger displacement is mainly distributed at the incident interface, and the value of $F(\tau)$ is also at a negligible level. Subsequently, an obvious

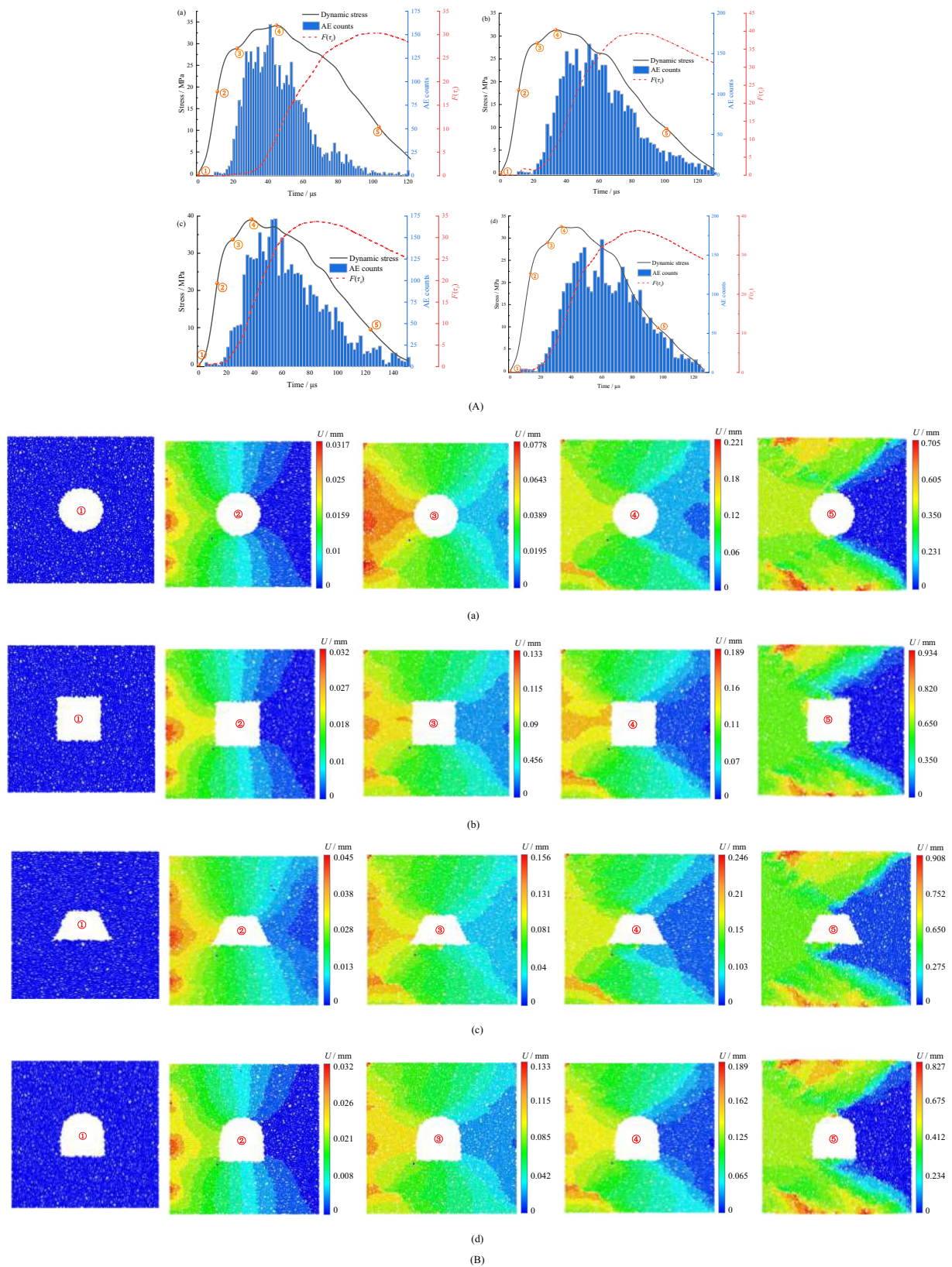


Fig. 8 **A** Dynamic stress histories and AE characteristics and **B** Displacement contours of specimens containing a (a) circle, (b) square, (c) trapezoidal and (d) arched hole at featured points

drop in dynamic stress is observed (③), accompanied by a large number of AE events that result a surge in AE counts. The time function $F(\tau)$ soars as well, which further indicates that microcrack cumulation is sufficient to induce macro crack emergence. At this point, displacement is symmetrically distributed in a semi-triangle along the median. Figure 8a③ shows that the left sidewall of the circular hole bears the largest displacement, followed by the roof and floor, while the right sidewall exhibits the minimum displacement. A potential X-shaped crack trajectory gradually forms along the diagonal of the specimen. As dynamic stress peaks at point ④, the number of AE events starts to decrease but remains relatively high. The displacement triangle at the incident side narrows, leading to a concentration at the middle part of the circular hole, whereas its counterpart at the transmitted side expands towards the upper and lower boundaries of the hole, as shown in Fig. 8a④. The growth rate of $F(\tau)$ nearly reaches the maximum value before exhibiting a decreasing trend; however, its absolute quantity still rises. In addition, a secondary crack is generated at the lower part near the incident interface. Upon the dynamic stress entering the post-peak stage, AE counts experience a prominent decrease, dropping to less than 10 after 100 μ s, indicating that the dominant cracks that split the entire structure of the specimen have taken shape, which is supported by the displacement contour in Fig. 8a⑤, at which $F(\tau)$ also shows a decreasing tendency. In Figs. 8b and c, both square- and trapezoidal-hole scenarios exhibit a similar dynamic cracking process to that of circular-hole scenario. However, sharp corners are prone to stress concentration. The main inclined crack at the hole roof is close to the midpoint of the side, while at the hole floor, the main crack initiates at the right corner and experience a slight diversion prior to the final extension along the specimen diagonal. Figure 8d presents the dynamic stress history coupled with AE counts and fracture process of specimens containing an arched hole, respectively. It can be observed that the displacement contours resemble those of the upper half part of circular-holed specimens as well as the lower half part of square-holed specimens. This enlightens us that, for arched shape, the most applied cross-section in engineering projects, both vault and lower right corner are vulnerable positions when subjected to dynamic loadings perpendicular to the central axis of tunnels/caverns.

Figure 9a manifests the dynamic stress, AE counts and $F(\tau)$ over time for specimens containing an elliptical hole with various inclination angles, and the corresponding failure process is shown in Fig. 9b. As the compressive wave reaches the specimen, the dynamic stress undergoes a linear increasing variation tendency with sporadic AE events, and the $F(\tau)$ also approaches 0. During the linearly elastic stage, a contrasting displacement gradient forms around the

left hole tip for inclination angles between 0° and 75° , as displayed in Figs. 9a–f②. However, for an inclination angle of 90° , the gradient is along the left periphery of the elliptical hole (Fig. 9g②). As the inclination angle increases, the displacement gradient gradually moves up forward from the tip to the central hole area, and stress concentration at the hole tip is mitigated. With a continuous increase in dynamic stress, larger displacement tends to concentrate at the left side of the elliptical hole, while lower displacement is mainly distributed at its right side. The dividing interfaces suggest the following dominant macro crack paths (Fig. 9a–f③–④). During this stage, more AE activities are activated, giving rise to a significant increase in AE counts and $F(\tau)$. Based on the displacement contour in the latter unloading stage (Fig. 9a–f⑤), it can be found that the main cracks are shear cracks along the diagonal direction of the specimen, with the various initiation positions, from near the central part of the hole for the inclination angle no less than 45° to the hole tips for the inclination angle between 60° and 90° . Both AE counts and $F(\tau)$ exhibit a decreasing tendency in this phase, indicating that the specimen cannot bear further external loadings due to final collapse.

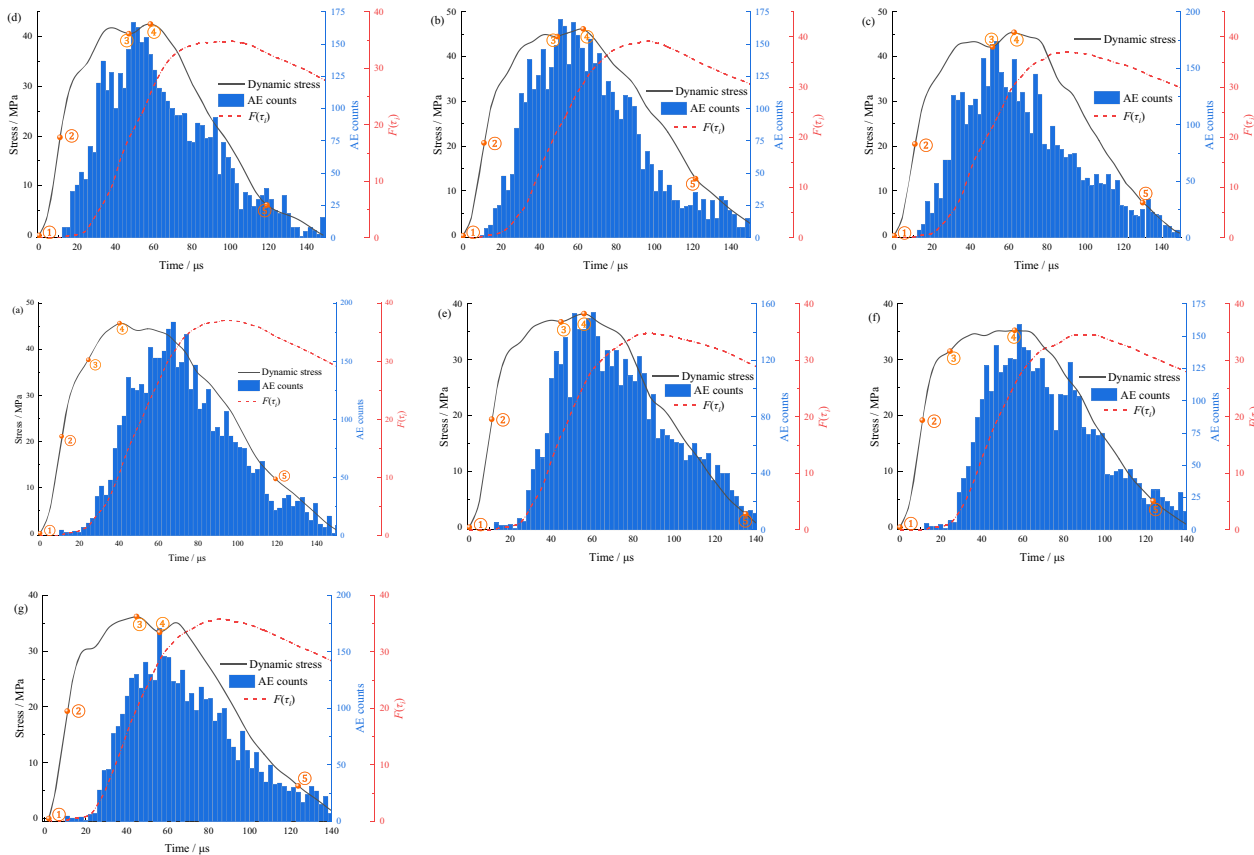
4.3 Failure mode

Ultimate failure modes of intact and pre-holed specimens after dynamic uniaxial compression are depicted in Fig. 10. For all types of specimens, tensile micro cracks play a dominant role in fracture process, indicating that shear macro cracks are more likely to be produced through multiple connection of tensile micro cracks, which is similar to the findings of Einstein and Dershowitz (1990). Shear micro cracks are also generated, but in small quantities, and can be further classified into two types: shear-tensile cracks, where the shear stress between two particles is less than cohesion; and shear-compressive cracks, where the shear stress exceeds cohesion. In addition, both micro and macro cracks are concentrated on the upper and lower sides of the hole, resulting in a quasi-X or X-shaped failure pattern. Fewer cracks are distributed along the left and right sides of the hole.

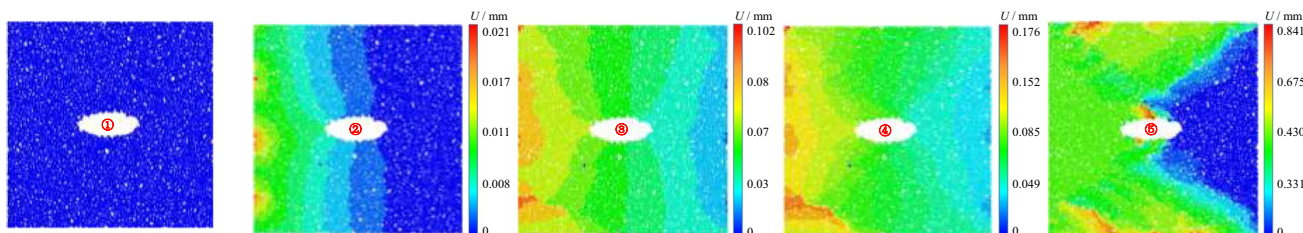
For specimens containing a circular hole, new macro shear cracks are usually generated at the roof and floor of the hole, and propagate along the diagonal direction of the specimen until they extend to specimen edges and form an X-shaped failure mode, as shown in Fig. 10b. For specimens containing a square (Fig. 10c) or an arched (Fig. 10e) hole, apart from corners, cracks are nearly uniformly distributed along the upper and lower sides of the hole. However, regarding a trapezoidal hole, cracks at the upper side are similar to those of the square hole, but the cracks at the lower part gradually accumulate towards the left corner, as shown in Fig. 10d. With respect to an elliptical hole, as the

inclination angle less than 45°, cracks not only gather at the hole tips but also near the hole perimeter, as displayed in Figs. 10f–i. Once the inclination angle exceeds 45°,

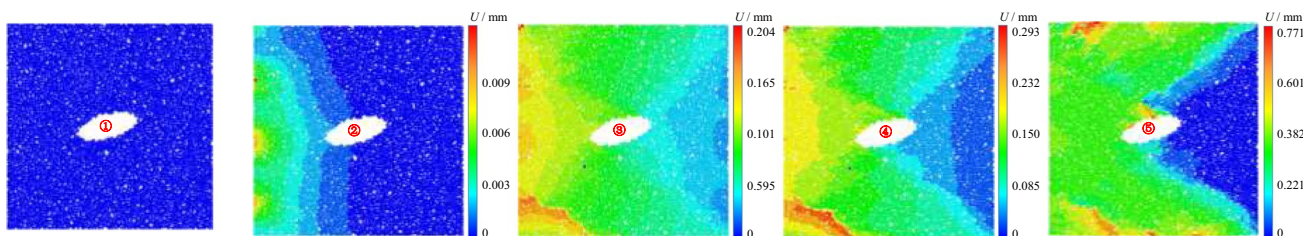
the cracks along the hole periphery gradually accumulate towards the hole tips, and they even almost disappear at an inclination angle of 90°.



(A)



(a)



(b)

Fig. 9 **a** Dynamic stress histories and AE characteristics and **b** Displacement contours at featured points of specimens containing an elliptical hole with the inclination angle from **a–g** 0°–90° at an interval of 15°

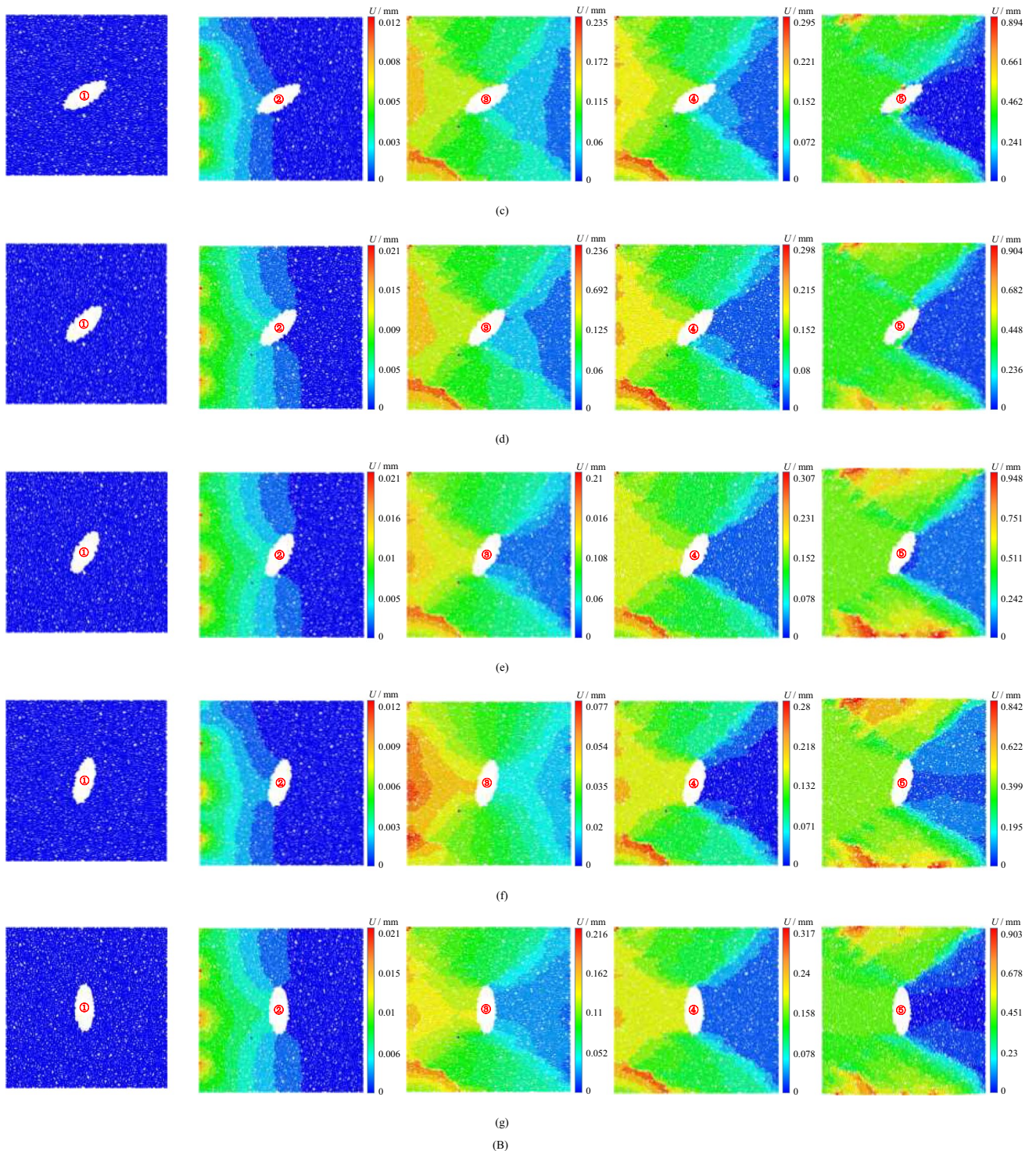


Fig. 9 (continued)

4.4 Energy analysis

Figure 11 shows the effect of hole shape on the energy properties of rock specimens, where the cumulative height of bars represents the incident energy. It can be observed

that the incident energy of an intact specimen is less than that of pre-holed specimens possessing a similar value. Reflected energy significantly increases as a hole is produced at the specimen center regardless of its shape. As the inclination angle of an elliptical hole rises, reflected

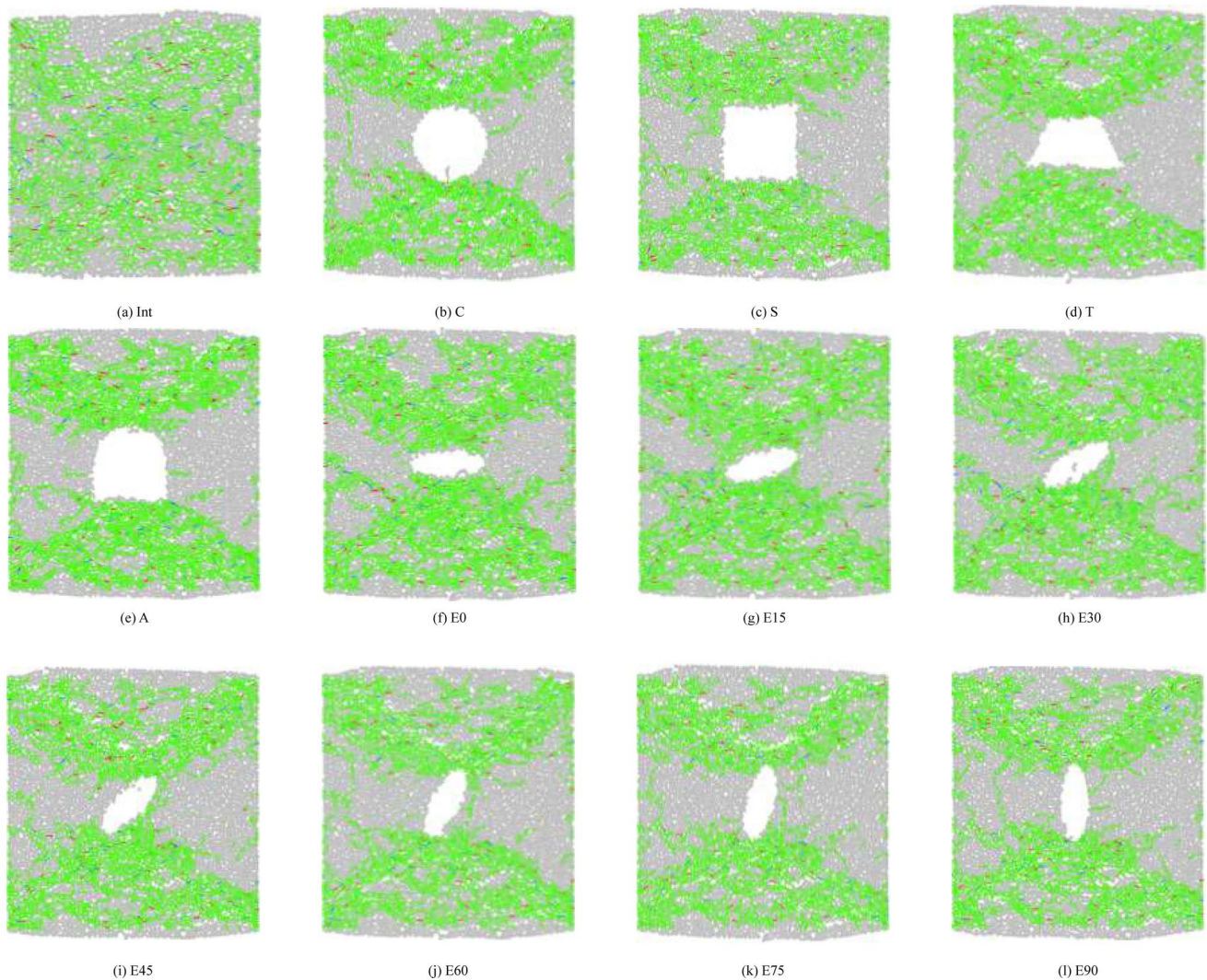


Fig. 10 Failure patterns of intact and pre-holed specimens (colors blue, red and green denote shear-compressive, shear-tensile and tensile microcracks, respectively)

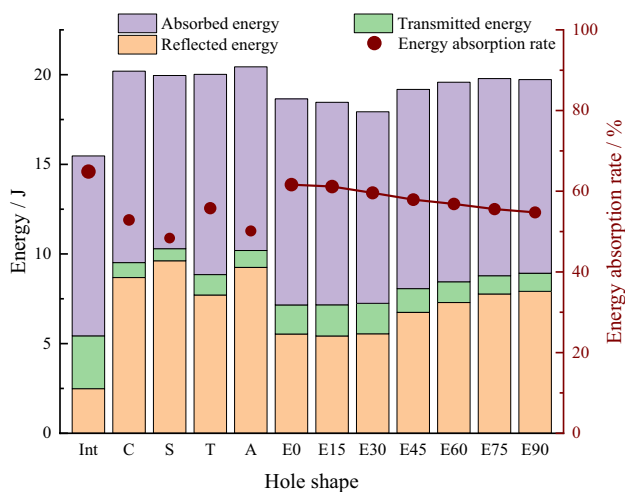


Fig. 11 Energy parameters of intact and pre-holed specimens

energy exhibits an increasing tendency, whereas transmitted energy first increases and then decreases, though it only occupies less than 10% of incident energy. The transmitted energy of an intact specimen is 2.95 J, and the creation of a hole reduces this value to less than 1 J for circle, square and arched holed specimens. Absorbed energy always accounts for the largest proportion in incident energy, and energy absorption rate (R) is introduced to evaluate the utilization rate of input energy that is employed to break the specimen:

$$R = \frac{E_A}{E_I} \tag{6}$$

where E_A and E_I denote absorbed energy and incident energy, respectively. Figure 11 indicates that intact specimens possess the largest energy absorption rate of 61.61%. For specimens containing a circle, square, trapezoidal

and arched hole, it drops to 52.88%, 48.40%, 55.79% and 50.14%, respectively. With the increasing inclination angle, the rate experiences a decreasing variation trend, which enlightens that engineering tunnels are more likely to collapse when the axial direction of the tunnel with an elliptical cross section is perpendicular to external loads. Hence, during the excavation of tunnels and caverns, both cross section and loading direction should be considered to ensure safe construction with minimum energy expenditure.

5 Discussion

5.1 Crack initiation analysis

To uncover the crack initiation mechanism, the force chain distribution of specimens just prior to macro crack initiation

is obtained and shown in Fig. 12. For an intact specimen, it can be seen from Fig. 12a that tensile force chains are approximately uniformly distributed in the specimen, indicating that this type of specimen can be regarded as a homogeneous material. For a circular hole, two quasi-triangle tensile areas are symmetrically formed at the flanks of the hole where following cracks are more likely to generate, and the remaining hole perimeter is in a compressive stress state, as displayed in Fig. 12b. For a square hole in Fig. 12c, tensile areas are similar to that of the circular hole but become larger. Lateral sides are subjected to tensile stress, but the top and bottom sides are covered by compressive stress. Notably, the four sharp corners also bear a tensile stress concentration. In Figs. 12d and e, tensile stresses also assemble at the later sides of the trapezoidal hole, whereas top and bottom zones are subjected to compressive stress. From above analysis, it can be concluded that side walls are prone to

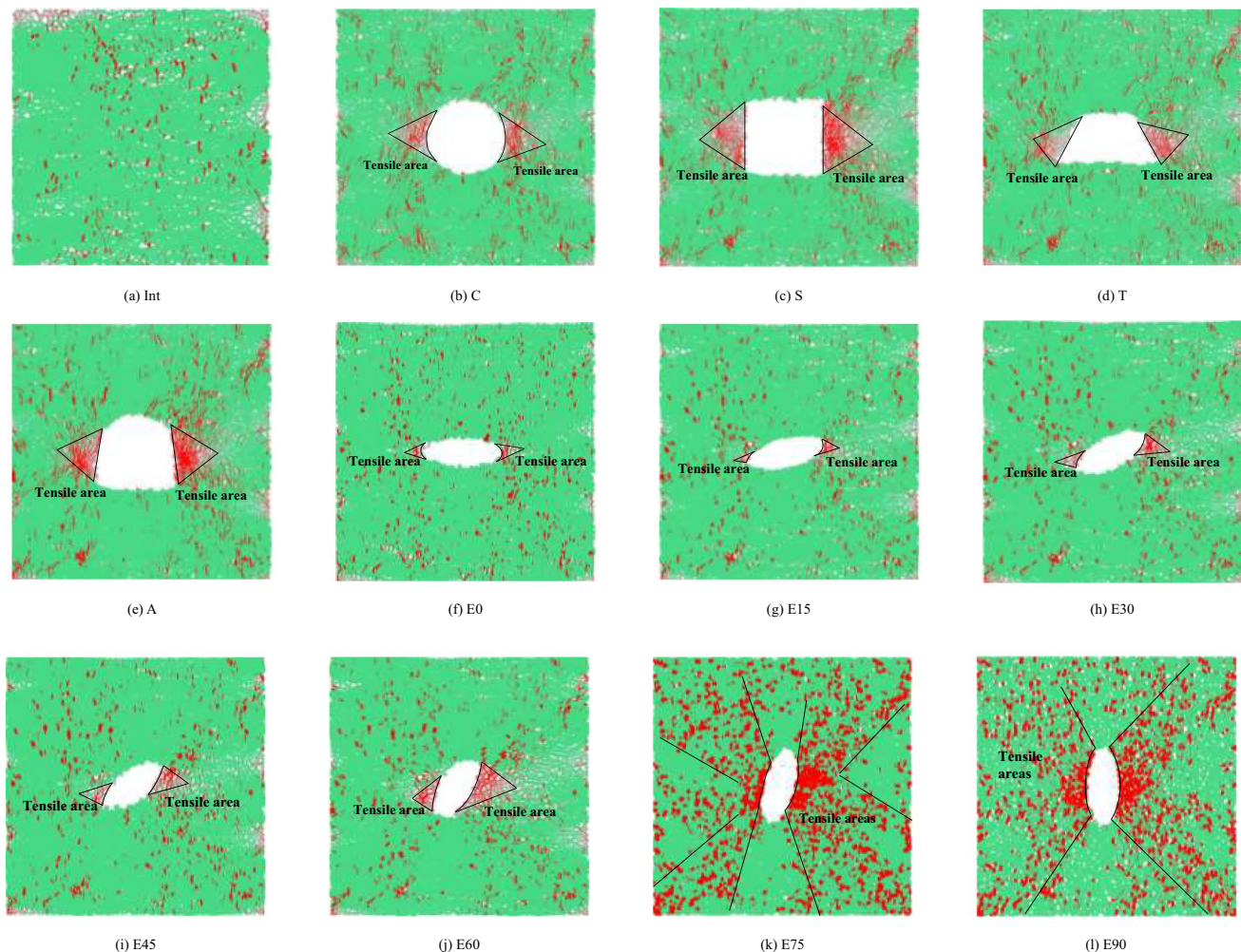


Fig. 12 Force chain distribution of intact and pre-holed specimens (colors red and green denote tensile and compressive stress, respectively)

dynamic failure when subjected to horizontal dynamic loads, at which supports should be strengthened to enhance the stability of excavation.

For an elliptical hole with the inclination angle of 0° in Fig. 12f, most of the hole periphery is under compression, apart from two small areas at the hole tip, where tensile stress plays a key role. However, with the increase of inclination angle, tensile concentrations gradually move from tips to the central part, but the tensile areas still include the tips before 45° . As the inclination angle reaches 45° , as shown in Fig. 12i, tensile areas are near the hole tips but do not cover the tips. With the continuous increase of inclination angle, the scope of tensile stress enlarges and nearly embraces the whole side walls for angles of 75° and 90° . Besides, tensile stress strips are also formed along the diagonal direction

of the specimen, as can be seen in Figs. 12k and l. Above discussion indicates that the larger the inclination angle is, the larger the affected area under tension is, and the after the hole tips are.

5.2 Post-failure fragmentation

To assess the degree of fracture in intact and pre-holed specimens, the number of microcracks after failure for all types of cracks is calculated and shown in Fig. 13. From Fig. 13a, it can be observed that intact specimens possess the largest quantity of micro cracks due to a relatively larger bearing area compared to other pre-holed specimens. Circular, square, trapezoidal, and arched holes significantly reduce the total crack number, but their quantities are similar.

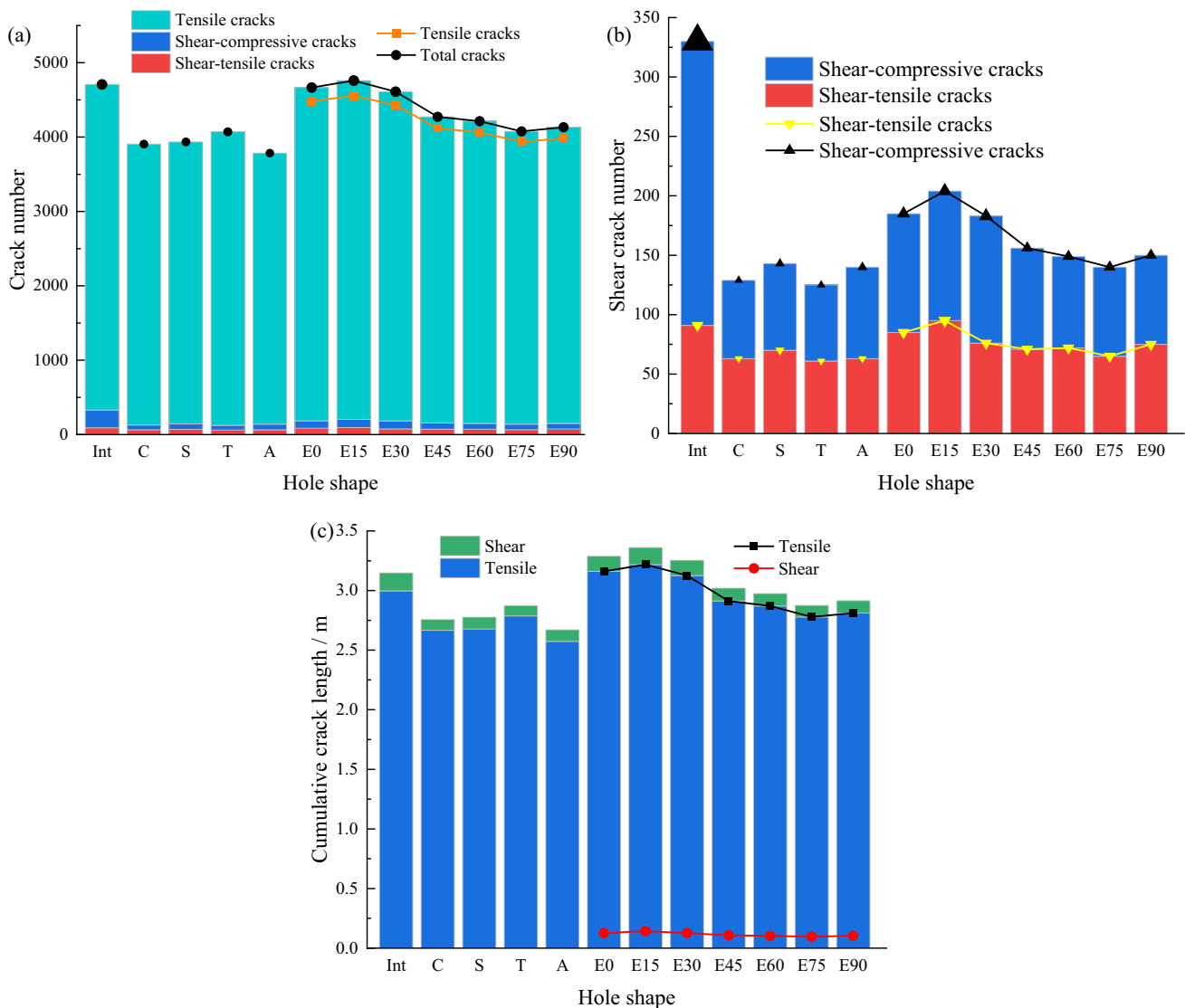


Fig. 13 a and b Micro crack number and c Cumulative crack length of intact and pre-holed specimens

In contrast, for an elliptical hole, as the inclination angle increases, the micro crack quantity initially increases to 4556 at 15° , the largest value, before exhibiting a decreasing tendency followed by a minor increase between 75° and 90° . It is noteworthy that specimens containing an elliptical hole at 0° – 30° have more microcracks than intact specimens, indicating that these specimens experience a dramatic rupture, as shown in Fig. 13. The proportion of tensile micro cracks occupies a dominant position and remarkably exceeds the shear counterpart regardless of hole shape. This suggests that tensile stress plays a crucial role in rock breaking and that the essential mechanism of cracks at a micro scale is tension. The tensile crack number for specimens containing a square and trapezoidal hole is larger than that for circular- and arched- holed specimens due to sharp corners being susceptible to stress concentration which further induces more tensile micro cracks. The trend of tensile crack number versus inclination angle for specimens with an elliptical hole is similar to that of total micro crack number.

The numbers of shear-compressive and shear-tensile cracks under various hole shapes are illustrated in Fig. 13b. The quantify of shear cracks in intact specimens is much higher than other specimens, indicating that the existence of a pre-hole can reduce shear stress within the specimen. The number of shear cracks in circular- and trapezoidal- holed specimens is marginally smaller than in square- and arch-holed specimens. With respect to specimens with an elliptical hole, the quantity of shear cracks also first increases, peaks at 15° , and then decreases. The number of shear-tensile cracks is similar for circular-, square-, trapezoidal-, and arched- holed specimens but lower than that of intact specimens. The effect of inclination angle of the elliptical hole on the quantity of shear-tensile is minor, in addition to that for a 15° specimen, which is even slightly larger than that of intact specimens. However, its effect on shear-compressive crack quantity is more prominent, exhibiting a first-increase-and-then-decrease trend with the largest value at 15° , but all quantities are significantly lower than of intact specimens. The number of shear-compressive cracks in circular- and trapezoidal- holed specimens is smaller than that in square- and arch- holed specimens. In summary, pre-hole greatly reduces the generation of shear cracks, which further promotes a tensile-dominant failure at micro scale.

Figure 13c displays the effect of hole shape on cumulative crack length. The cumulative shear, tensile and total crack length in an intact specimen is 0.15, 3.0 and 3.15 m, respectively. In addition to specimens containing an elliptical hole, other types of the hole lead to a distinct reduction in these micro crack lengths, among which the trapezoidal hole results in the highest maximum lengths for both total and tensile cracks, whereas the square hole produces the longest shear crack length. Regarding the inclination angle of the elliptical hole, all three crack length parameters show

a conspicuous increase from 0° to 15° prior to decreasing overall for angles between 15° and 90° . When the angle is less than 30° , the cumulative lengths of both tensile and total cracks outweigh that of intact specimens, indicating a more severe fragmentation after failure.

5.3 Crack type determination

According to the dynamic fracture process, inclined macro shear cracks are produced in all types of specimens. Herein the specimen containing an arched hole is taken as an example to analyze the attributes of these inclined macro shear cracks. Figure 14a presents the particle velocity vector field of the arch-holed specimen prior to macro failure. Similar to displacement trend lines (Zhang and Wong 2014) (Fig. 14c), velocity trend arrows are introduced to identify the crack mechanism, where the color and direction of these arrows represent the magnitude and extending direction of macro cracks. It is observed that inclined macro cracks belong to a DF_III type due to significant differences in both magnitude and direction, which induces slipping behavior to generate shear cracks. However, a crack near the left corner can be identified as a DF-I type, where particles move in completely opposite directions despite possessing similar magnitudes. The corresponding contact force distribution is presented in Fig. 14b, which shows that principal stress at inclined crack areas is much larger than other areas. This driving stress gives rise to dominant macro shear crack development during dynamic failure process of pre-holed specimens, even though they are subjected to tensile stress at a micro scale.

5.4 Comparative analysis of fracture behavior under static and dynamic compression

Zeng et al. (2018) conducted a numerical study on the effect of hole shape on the fracture behavior of rock specimens under static uniaxial compression. The failure patterns of these specimens are in Fig. 15a, revealing the presence of inclined shear cracks. However, these cracks are not purely along the diagonal direction of the specimen, unlike those under dynamic axial compression, as depicted in Fig. 9b. In addition, dominant cracks initiate from both sidewalls of the hole under static loads but from the roof and floor of the hole subjected to dynamic loads. Tensile cracks from the top and bottom areas of the hole are also detected in those specimens under static compression. Similarly, such cracks are generated in those under dynamic loads but only one at the left floor corner. Moreover, shear cracks form an X-shaped pattern around the hole under dynamic loading conditions, while only half of an

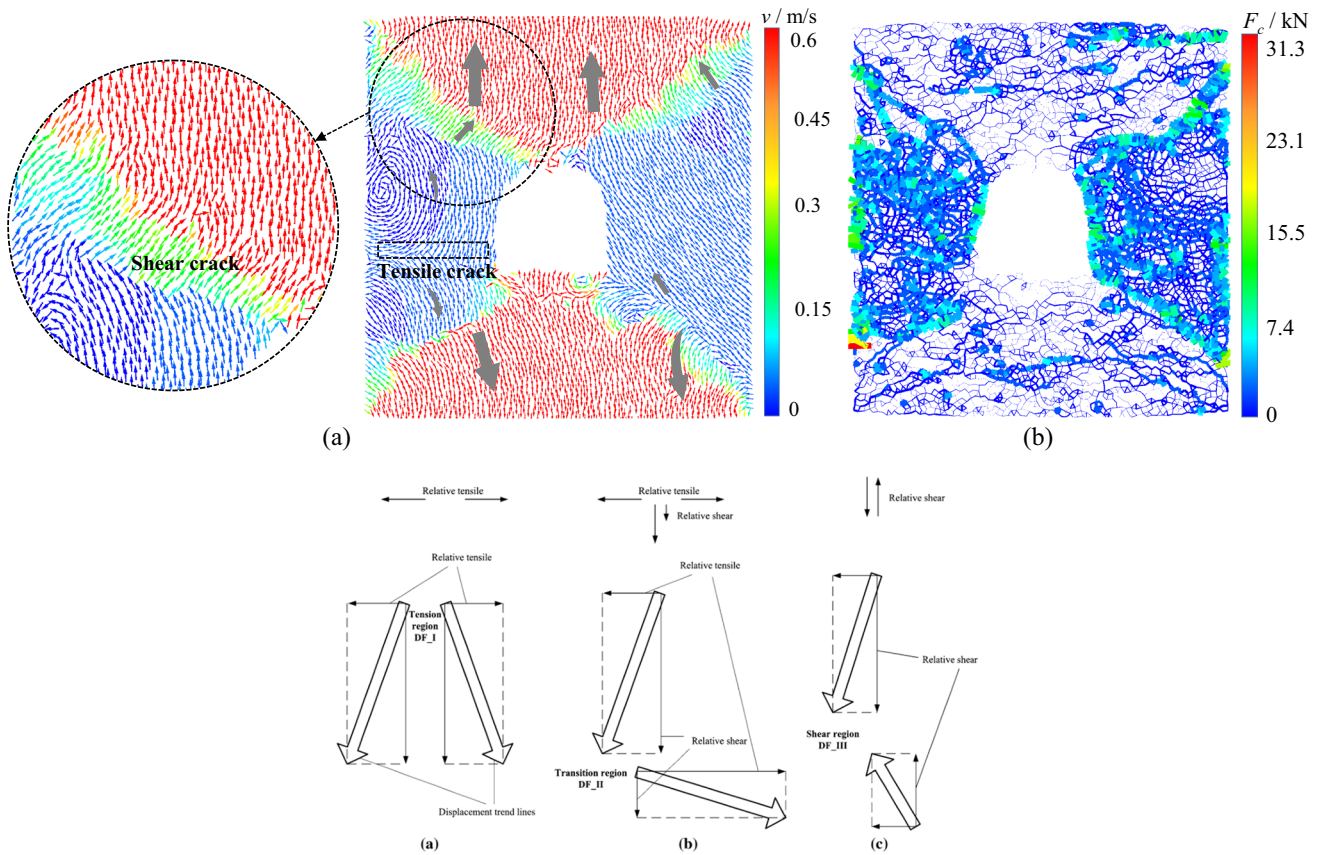


Fig. 14 **a** Particle velocity vector field and **b** Contact force distribution (F_c) of the arch-holed specimen prior to macro failure, and **c** Crack types defined by displacement trend lines (thick open arrows) (Zhang and Wong 2014)

X-shape crack is observed under static loading conditions except for specimens with an elliptical hole (E0).

Dynamic crack growth of rock specimens containing an elliptical/circular hole was experimentally examined by Cheng (2015), and Fig. 15b displays the results of failure patterns. Its comparison with Fig. 9b indicates that numerical results agree well with experimental results, further affirming the reliability of this study, especially for other types of specimens. Notably, the failure mode of the specimen with a 45° elliptical hole is slightly distinct from its numerical counterpart, which may be caused by the heterogeneity of rock materials and unevenness of edges.

6 Conclusions

A numerical investigation was carried out to study the dynamic mechanical behavior of rock specimens containing a hole with various shapes. AE characteristics, displacement contour, micro crack pattern and force chain distribution during the loading process were monitored and discussed

to clarify the fracture process from crack initiation to final failure. The following conclusions were drawn:

- (1) The presence of a hole significantly reduces the dynamic uniaxial compressive strength of rocks, with elliptical hole at a 15° angle having the lowest reduction by 22.97% and square hole exhibiting the highest reduction by 49.68%, compared with the intact specimen. However, the peak strain demonstrates a totally different variation trend, with the arched holed specimen experiencing a dramatic reduction from 0.0682% (intact specimen) to 0.0180% and the 30° elliptical holed specimen displaying a prominent increase to 0.106% that exceeds intact specimens (0.0682%).
- (2) Regardless of the shape of the aperture, the dynamic failure process is primarily governed by the propagation of shear cracks along the diagonal direction of the specimen. This phenomenon can be identified by the particle velocity vector field and the contact force distribution.

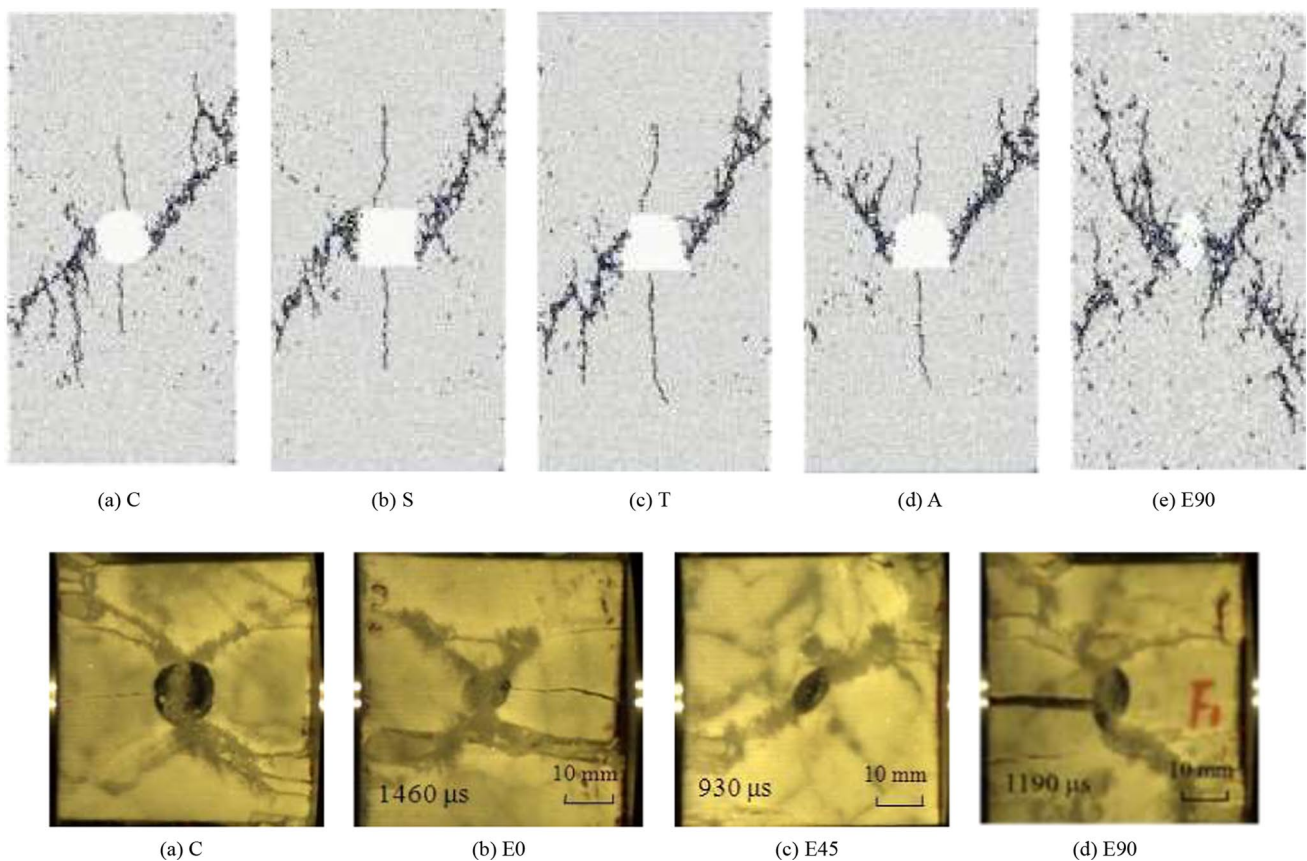


Fig. 15 **a** Numerical failure modes of perforated specimens under static uniaxial compression (Zeng et al. 2018) and **b** Experimental failure modes of perforated specimens under dynamic uniaxial compression (Cheng 2015)

- (3) Energy absorption rate, positively correlated with the dynamic strength, is the underlying mechanism driving the dynamic crack development.
- (4) The quantity of micro shear cracks is greatly reduced for pre-holed specimens, while the counterpart of micro tensile cracks is closely related to the hole shape.
- (5) Primary crack paths are mainly along both sidewalls of the hole under static loads, whereas they finally form at the roof and floor of the hole when exposed to dynamic loads.

Acknowledgements This research was financially supported by the Postgraduate Research & Practice Innovation Program of Jiangsu Province (KYCX21_0119), National Natural Science Foundation of China (52074349 and 52304113) and China Scholarship Council (CSC) Scholarship (202106090203).

Declarations

Conflict of interest The authors declare that they have no conflict of interest.

Open Access This article is licensed under a Creative Commons Attribution 4.0 International License, which permits use, sharing,

adaptation, distribution and reproduction in any medium or format, as long as you give appropriate credit to the original author(s) and the source, provide a link to the Creative Commons licence, and indicate if changes were made. The images or other third party material in this article are included in the article's Creative Commons licence, unless indicated otherwise in a credit line to the material. If material is not included in the article's Creative Commons licence and your intended use is not permitted by statutory regulation or exceeds the permitted use, you will need to obtain permission directly from the copyright holder. To view a copy of this licence, visit <http://creativecommons.org/licenses/by/4.0/>.

References

- Abharian S, Sarfarazi V, Marji MF, Rasekh H (2022) Experimental and numerical evaluation of the effects of interaction between multiple small holes and a single notch on the mechanical behavior of artificial gypsum specimens. *Theor Appl Fract Mech*. <https://doi.org/10.1016/j.tafmec.2022.103462>
- Ai S-G, Gao K (2023) Elastoplastic damage modeling of rock spalling/failure induced by a filled flaw using the material point method (MPM). *Rock Mech Rock Eng*. <https://doi.org/10.1007/s00603-023-03265-8>

- Carter BJ, Lajtai EZ, Petukhov A (1991) Primary and remote fracture around underground cavities. *Int J Numer Anal Met* 15:21–40. <https://doi.org/10.1002/nag.1610150103>
- Carter BJ, Lajtai EZ, Yuan Y (1992) Tensile fracture from circular cavities loaded in compression. *Int J Fract* 57:221–236. <https://doi.org/10.1007/bf00035074>
- Cheng T (2015) Experimental study on dynamic strength characteristics and crack propagation behavior of rock specimens with a single hole under impact loading. Central South University, Changsha
- Einstein HH, Dershowitz WS (1990) Tensile and shear fracturing in predominantly compressive stress fields: a review. *Eng Geol* 29:149–172. [https://doi.org/10.1016/0013-7952\(90\)90004-k](https://doi.org/10.1016/0013-7952(90)90004-k)
- Fakhimi A, Carvalho F, Ishida T, Labuz JF (2002) Simulation of failure around a circular opening in rock. *Int J Rock Mech Min Sci* 39:507–515. [https://doi.org/10.1016/S1365-1609\(02\)00041-2](https://doi.org/10.1016/S1365-1609(02)00041-2)
- Han Z, Li D, Zhou T, Zhu Q, Ranjith PG (2020) Experimental study of stress wave propagation and energy characteristics across rock specimens containing cemented mortar joint with various thicknesses. *Int J Rock Mech Min Sci* 131:104352. <https://doi.org/10.1016/j.ijrmms.2020.104352>
- Han Z, Li D, Li X (2022a) Experimental study on the dynamic behavior of sandstone with coplanar elliptical flaws from macro, meso, and micro viewpoints. *Theor Appl Fract Mech* 120:103400. <https://doi.org/10.1016/j.tafmec.2022.103400>
- Han Z, Xie S, Li D (2022b) Discrete element study on the mechanical behavior of flawed rocks under dynamic compression. *Theor Appl Fract Mech* 121:103516. <https://doi.org/10.1016/j.tafmec.2022.103516>
- Han Z, Li D, Li X (2022) Dynamic mechanical properties and wave propagation of composite rock-mortar specimens based on SHPB tests. *Int J Min Sci Technol* 32(4):793–806
- Han Z, Li J, Wang H, Zhao J (2023) Initiation and propagation of a single internal 3D crack in brittle material under dynamic loads. *Eng Fract Mech* 285:109299
- Huang Y-H, Yang S-Q, Ranjith PG, Zhao J (2017) Strength failure behavior and crack evolution mechanism of granite containing pre-existing non-coplanar holes: experimental study and particle flow modeling. *Comput Geotech* 88:182–198. <https://doi.org/10.1016/j.compgeo.2017.03.015>
- Inglis CE (1913) Stress in a plate due to the presence of cracks and sharp corners. *Trans Inst Naval Archit* 55:219–241
- Jongpradist P, Tunsakul J, Kongkitkul W, Fadsiri N, Arangelovski G, Youwai S (2015) High internal pressure induced fracture patterns in rock masses surrounding caverns: experimental study using physical model tests. *Eng Geol* 197:158–171. <https://doi.org/10.1016/j.enggeo.2015.08.024>
- Karimi-Khajelangi B, Noorian-Bidgoli M (2022) Numerical study of the effect of rock anisotropy on stresses around an opening located in the fractured rock mass. *J Pet Sci Eng*. <https://doi.org/10.1016/j.petrol.2021.109593>
- Khazaei C, Hazzard J, Chalaturnyk R (2015) Damage quantification of intact rocks using acoustic emission energies recorded during uniaxial compression test and discrete element modeling. *Comput Geotech* 67:94–102. <https://doi.org/10.1016/j.compgeo.2015.02.012>
- Kooi CB, Verruijt A (2001) Interaction of circular holes in an infinite elastic medium. *Tunn Undergr Space Technol* 16:59–62. [https://doi.org/10.1016/s0886-7798\(01\)00027-x](https://doi.org/10.1016/s0886-7798(01)00027-x)
- Lajtai EZ, Lajtai VN (1975) The collapse of cavities. *Int J Rock Mech Min Sci* 12:81–86. [https://doi.org/10.1016/0148-9062\(75\)90001-7](https://doi.org/10.1016/0148-9062(75)90001-7)
- Li XB, Zou Y, Zhou ZL (2014) Numerical simulation of the rock SHPB test with a special shape striker based on the discrete element method. *Rock Mech Rock Eng* 47:1693–1709. <https://doi.org/10.1007/s00603-013-0484-6>
- Li D, Zhu Q, Zhou Z, Li X, Ranjith PG (2017) Fracture analysis of marble specimens with a hole under uniaxial compression by digital image correlation. *Eng Fract Mech* 183:109–124. <https://doi.org/10.1016/j.engfracmech.2017.05.035>
- Li D, Han Z, Sun X, Zhou T, Li X (2019) Dynamic mechanical properties and fracturing behavior of marble specimens containing single and double flaws in SHPB tests. *Rock Mech Rock Eng* 52:1623–1643. <https://doi.org/10.1007/s00603-018-1652-5>
- Li Y, Yang S-Q, Li Y (2021) Experiment and numerical simulation on cracking behavior of marble containing double elliptical holes under uniaxial compression. *Theor Appl Fract Mech* 112:102928. <https://doi.org/10.1016/j.tafmec.2021.102928>
- Li J, Yuan W, Li H, Zou C (2022) Study on dynamic shear deformation behaviors and test methodology of sawtooth-shaped rock joints under impact load. *Int J Rock Mech Min Sci* 158:105210. <https://doi.org/10.1016/j.ijrmms.2022.105210>
- Li H et al (2023a) Effect of water saturation on dynamic behavior of sandstone after wetting-drying cycle treatment. *Eng Geol*. <https://doi.org/10.1016/j.enggeo.2023.107105>
- Li P, Cai M, Gao Y, Wang P, Miao S, Wang Y, Xi X (2023b) Dynamic mechanical behavior and cracking mechanism of cross-jointed granite containing a hole. *J Mater Res Technol* 22:1572–1594. <https://doi.org/10.1016/j.jmrt.2022.12.034>
- Liu B, Zhou Y, Gao Y-T, Xu C (2020) Experimental and numerical study on crack development characteristics between two cavities in rock-like material under uniaxial compression. *Theor Appl Fract Mech* 109:102755. <https://doi.org/10.1016/j.tafmec.2020.102755>
- Mahanta B, Tripathy A, Vishal V, Singh TN, Ranjith PG (2017) Effects of strain rate on fracture toughness and energy release rate of gas shales. *Eng Geol* 218:39–49. <https://doi.org/10.1016/j.enggeo.2016.12.008>
- Mahmoodzadeh A, Nejati HR, Mohammadi M, Salih Mohammed A, Hashim Ibrahim H, Rashidi S (2022) Numerical and Machine learning modeling of hard rock failure induced by structural planes around deep tunnels. *Eng Fract Mech*. <https://doi.org/10.1016/j.engfracmech.2022.108648>
- Poulsen BA, Adhikary D, Guo H (2018) Simulating mining-induced strata permeability changes. *Eng Geol* 237:208–216. <https://doi.org/10.1016/j.enggeo.2018.03.001>
- Ramesh KT, Hogan JD, Kimberley J, Stickle A (2015) A review of mechanisms and models for dynamic failure, strength, and fragmentation. *Planet Space Sci* 107:10–23. <https://doi.org/10.1016/j.pss.2014.11.010>
- Sagong M, Park D, Yoo J, Lee JS (2011) Experimental and numerical analyses of an opening in a jointed rock mass under biaxial compression. *Int J Rock Mech Min Sci* 48:1055–1067. <https://doi.org/10.1016/j.ijrmms.2011.09.001>
- Sammis CG, Ashby MF (1986) The failure of brittle porous solids under compressive stress states. *Acta Metall* 34:511–526. [https://doi.org/10.1016/0001-6160\(86\)90087-8](https://doi.org/10.1016/0001-6160(86)90087-8)
- Setiawan NB, Zimmerman RW (2020) A unified methodology for computing the stresses around an arbitrarily-shaped hole in isotropic or anisotropic materials. *Int J Solids Struct* 199:131–143. <https://doi.org/10.1016/j.ijsolstr.2020.03.022>
- Sharma DS (2012) Stress distribution around polygonal holes. *Int J Mech Sci* 65:115–124. <https://doi.org/10.1016/j.ijmecsci.2012.09.009>
- Tan L, Ren T, Dou L, Yang X, Cai X, Qiao M (2021a) Analytical stress solution for rock mass containing two holes based on an improved Schwarz alternating method. *Theor Appl Fract Mech* 116:103092. <https://doi.org/10.1016/j.tafmec.2021.103092>
- Tan L, Ren T, Dou L, Yang X, Qiao M, Peng H (2021b) Analytical stress solution and mechanical properties for rock mass containing a hole with complex shape. *Theor Appl Fract Mech* 114:103002. <https://doi.org/10.1016/j.tafmec.2021.103002>

- Tan L, Zhou Z, Cai X, Rui Y (2022) Analysis of mechanical behaviour and fracture interaction of multi-hole rock mass with DIC measurement. Measurement. <https://doi.org/10.1016/j.measurement.2022.110794>
- Tao M, Zhao H, Momeni A, Wang Y, Cao W (2020) Fracture failure analysis of elliptical hole bored granodiorite rocks under impact loads. Theor Appl Fract Mech 107:102516. <https://doi.org/10.1016/j.tafmec.2020.102516>
- Tao M, Zhao H, Momeni A, Cao W, Zhao Y (2022) Dynamic failure behavior and damage evolution process of holed sandstone under impact loads. Int J Damage Mech. <https://doi.org/10.1177/10567895221123092>
- Ukadgaonker VG (1980) Stress analysis of a plate containing two circular holes having tangential stresses. AIAA J 18:125–128. <https://doi.org/10.2514/3.7642>
- Wang S, Li X (2017) Dynamic distribution of longwall mining-induced voids in overlying strata of a coalbed. Int J Geomech 17:04016124
- Weng L, Li X, Taheri A, Wu Q, Xie X (2017) Fracture evolution around a cavity in brittle rock under uniaxial compression and coupled static–dynamic loads. Rock Mech Rock Eng 51:531–545. <https://doi.org/10.1007/s00603-017-1343-7>
- Wu H, Zhao G, Liang W (2020) Mechanical properties and fracture characteristics of pre-holed rocks subjected to uniaxial loading: a comparative analysis of five hole shapes. Theor Appl Fract Mech. <https://doi.org/10.1016/j.tafmec.2019.102433>
- Xia Y et al (2023) Mechanism of excavation-induced cracking of the protective layer of a rock bench in a large underground powerhouse under high tectonic stress. Eng Geol. <https://doi.org/10.1016/j.enggeo.2022.106951>
- Xie H, Zhang Y, Chen Y, Peng Q, Liao Z, Zhu J (2021) A case study of development and utilization of urban underground space in Shenzhen and the Guangdong-Hong Kong-Macao Greater Bay Area. Tunn Undergr Space Technol 107:103651. <https://doi.org/10.1016/j.tust.2020.103651>
- Yan Z, Dai F, Liu Y, Li A, Du H (2021) Numerical assessment of the rate-dependent cracking behaviours of single-flawed rocks in split Hopkinson pressure bar tests. Eng Fract Mech 247:107656. <https://doi.org/10.1016/j.engfracmech.2021.107656>
- Yang S-Q, Yin P-F, Zhang Y-C, Chen M, Zhou X-P, Jing H-W, Zhang Q-Y (2019) Failure behavior and crack evolution mechanism of a non-persistent jointed rock mass containing a circular hole. Int J Rock Mech Min Sci 114:101–121. <https://doi.org/10.1016/j.ijrmms.2018.12.017>
- Yuan W, Wang X, Wang X-B (2020) Numerical investigation on effect of confining pressure on the dynamic deformation of sandstone. Eur J Environ Civ Eng 26:3744–3761
- Zeng W, Yang S-Q, Tian W-L (2018) Experimental and numerical investigation of brittle sandstone specimens containing different shapes of holes under uniaxial compression. Eng Fract Mech 200:430–450. <https://doi.org/10.1016/j.engfracmech.2018.08.016>
- Zhang X-P, Wong LNY (2014) Displacement field analysis for cracking processes in bonded-particle model. Bull Eng Geol Environ 73:13–21. <https://doi.org/10.1007/s10064-013-0496-1>
- Zhang LQ, Yue ZQ, Lee CF, Tham LG, Yang ZF (2003) Stress solution of multiple elliptic hole problem in plane elasticity. J Eng Mech 129:1394–1407. [https://doi.org/10.1061/\(asce\)0733-9399\(2003\)129:12\(1394\)](https://doi.org/10.1061/(asce)0733-9399(2003)129:12(1394))
- Zhang Q, Wang X, Tian L, Huang D (2018) Analysis of mechanical and acoustic emission characteristics of rock materials with double-hole defects based on particle flow code. Shock Vib 2018:1–11
- Zhang X-P, Ji P-Q, Peng J, Wu S-C, Zhang Q (2020) A grain-based model considering pre-existing cracks for modelling mechanical properties of crystalline rock. Comput Geotech. <https://doi.org/10.1016/j.compgeo.2020.103776>
- Zhang B, Zhu P, Zhang J, Li S, Qiu D, Li J (2022a) Effect of an adjacent flaw on the crack propagation of a horseshoe-shaped cavity. Rock Mech Rock Eng 56:1807–1821. <https://doi.org/10.1007/s00603-022-03132-y>
- Zhang K, Jiang Z, Liu X, Zhang K, Zhu H (2022b) Quantitative characterization of the fracture behavior of sandstone with inclusions: experimental and numerical investigation. Theor Appl Fract Mech 121:103429. <https://doi.org/10.1016/j.tafmec.2022.103429>
- Zhang S, Cao H, Hu Q, Peng S, Zhang X (2023) Failure mechanism of rock specimens with an elliptical pre-hole under different stress conditions. Theor Appl Fract Mec 128:104133. <https://doi.org/10.1016/j.tafmec.2023.104133>
- Zhao G, Yang S (2015) Analytical solutions for rock stress around square tunnels using complex variable theory. Int J Rock Mech Min Sci 80:302–307. <https://doi.org/10.1016/j.ijrmms.2015.09.018>
- Zhao C, Matsuda H, Morita C, Shen MR (2011) Study on failure characteristic of rock-like materials with an open-hole under uniaxial compression. Strain 47:405–413. <https://doi.org/10.1111/j.1475-1305.2009.00701.x>
- Zhao ZL, Jing HW, Shi XS (2021) Experimental investigation and numerical modelling on strength and fracture behaviors of sandstone with weak distributed inclusions. Geotech Geol Eng 39:2521–2531. <https://doi.org/10.1007/s10706-020-01643-5>
- Zhao Y, Qi Q, Li J, Zhao Z, Li B (2023) Experimental investigations on the failure characteristics of brittle sandstone containing various heights of rectangle cavities under biaxial loading. Theor Appl Fract Mech. <https://doi.org/10.1016/j.tafmec.2023.103804>
- Zhou X, Zhang J, Yang S, Berto F (2021) Compression-induced crack initiation and growth in flawed rocks: a review. Fatigue Fract Eng Mater Struct 44:1681–1707. <https://doi.org/10.1111/ffe.13477>
- Zou C, Li J, Zhao X, Zhao J (2021) Why are tensile cracks suppressed under dynamic loading? Transition strain rate for failure mode. Extreme Mech Lett. <https://doi.org/10.1016/j.eml.2021.101506>

Publisher's Note Springer Nature remains neutral with regard to jurisdictional claims in published maps and institutional affiliations.